EXPERIMENTAL DETAILS

CHAPTER-III

EXPERIMENTAL DETAILS

This chapter deals with the synthesis of niobate based nanocrystalline sensor materials such as $InNbO_4$, $CrNbO_4$, $AlNbO_4$, $LaNbO_4$ and $FeNbO_4$ by niobium-citrate complex process and their physical characterization. Sensors developed for sensor studies for LPG, NH_3 and ethanol are studied in detail to know the sensitivity of the prepared materials.

3.1. MATERIALS USED

Materials used for the synthesis of Niobate based nanocrystalline sensor materials are given below.

- Niobium pentoxied [Nb_2O_5] (CDH)
- Aluminium nitrate [$Al(NO_3)_3$] (CDH)
- Indium nitrate [$In(NO_3)_3$] (CDH)
- Chromium nitrate [$Cr(NO_3)_3$] (Sd-fine)
- Ferric nitrate [$FeNO_3)_3$] (CDH)
- Lanthanum nitrate [$La(NO_3)_3$] (CDH)
- Citric acid [$C_6H_8O_7$] (CDH)
- Ammonium oxalate [$C_2H_8N_2O_4$] (E-Merck)
- Hydrogen fluoride [HF] (E-Merck)
- Ammonium Hydroxide [NH_4OH] (CDH)

3.2. Synthesis of $InNbO_4$ nanopowder

$InNbO_4$ nanopowder was obtained by low temperature niobium citrate complex process using following two steps. The first step was the preparation of hydrated Nb_2O_5 from Nb_2O_5. [12]. Nb_2O_5 was dissolved in HF to form $[NbOF_5]^{2-}$ or $[NbF_7]^{2-}$ complex. A freshly prepared aqueous solution of ammonium oxalate was added in excess and then aqueous NH_3 was added drop by drop to get hydrous niobium oxide ($Nb_2O_5.nH_2O$) as precipitated. (The flow chart of the synthesis of $Nb_2O_5.nH_2O$ is shown in Fig. 3.1). The precipitate of hydrous oxide was filtered and washed with 10% aqueous NH_3 solution by centrifugation to make the solution fluoride free hydrated Nb_2O_5. In the second step, the stoichiometry amount of hydrated Nb_2O_5 was dissolved in the aqueous solution of citric acid (2mol/mol of niobium ion) with the addition of catalytic amount of hydrogen peroxide, to get clear yellow coloured peroxo-citro-niobate. The addition of H_2O_2 promoted the solubility of the hydrated niobiate in citric acid and also shortened the required dissolution time. The clear solution of peroxo-citro-niobiate was mixed with stoichiometric amount of indium nitrate (mole ratio of In/Nb = 1:1) with constant stirring. The pH of the final solution mixture was adjusted to 7 by addition of aqueous NH_3. This mixture was heated at about 200 ^oC to get a dried black fluffy mass. This dried mass was calcined at 600 ^oC for 2 h to get $InNbO_4$ nanopowder. The resultant product was collected and subjected into both physical characterization and gas sensor studies. The flow chart of the synthesis of Indium niobate ($InNbO_4$) nano powder as shown in Fig. 3.2.

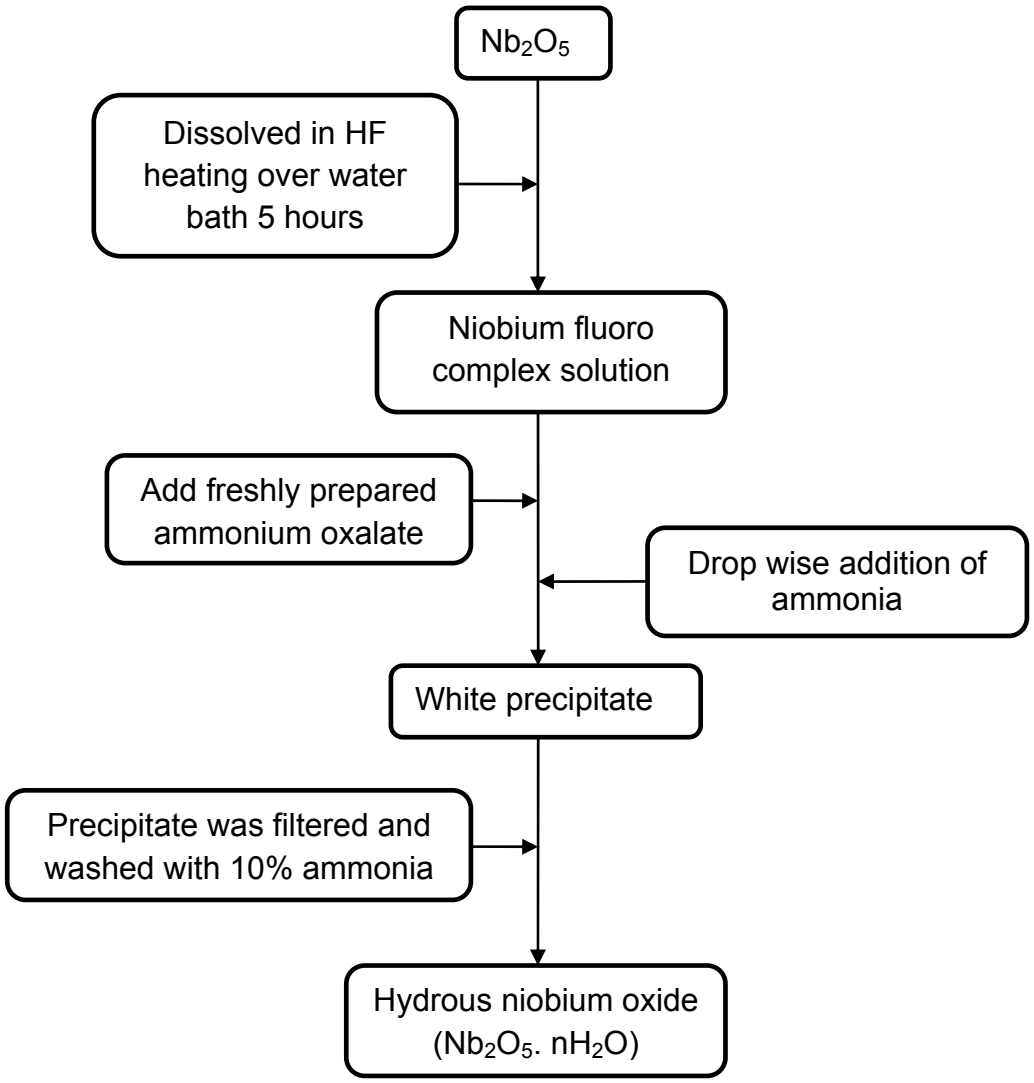

Fig. 3.1. Flow chart for preparation of $Nb_2O_5.nH_2O$

.

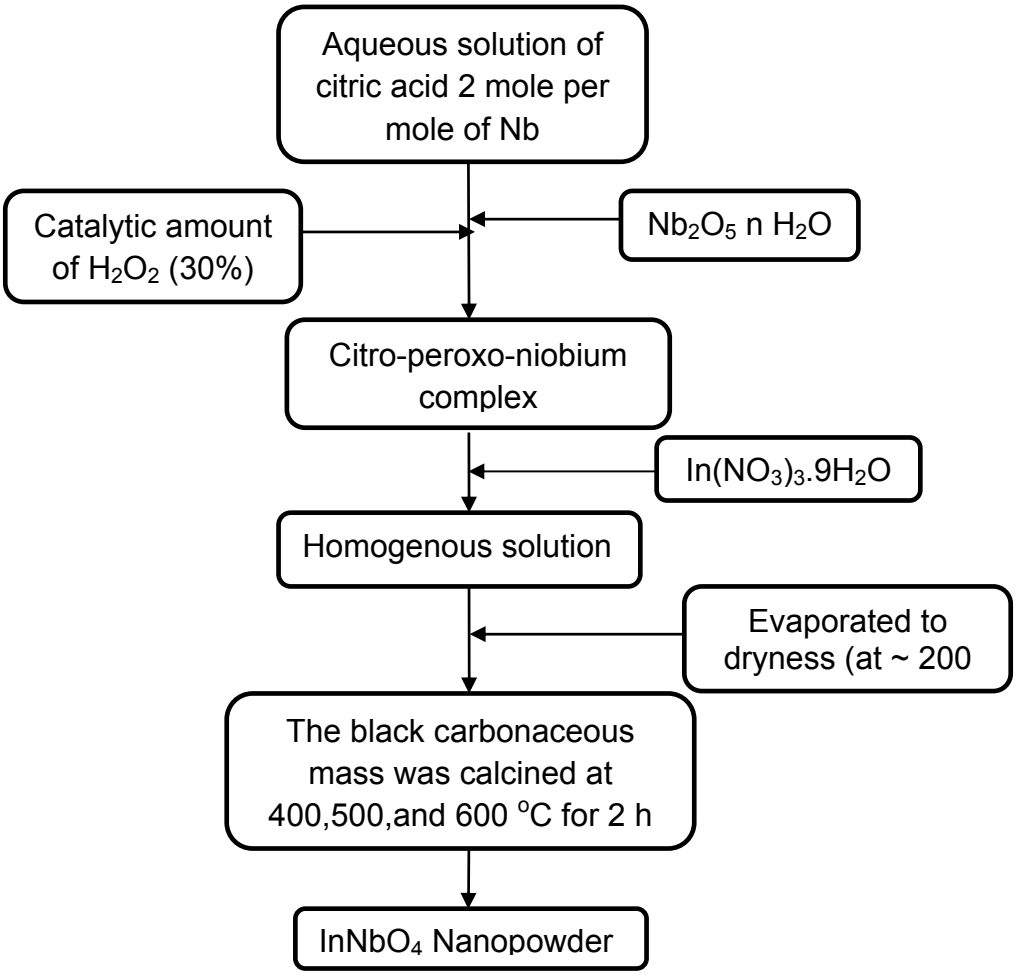

Fig. 3.2. Flow chart for preparation of $InNbO_4$ nanopowder by niobium-citrate complex process

3.3. Synthesis of $CrNbO_4$ nanopowder

$CrNbO_4$ nanopowder was obtained by low temperature niobium citrate complex process using following two steps. The first step was the preparation of hydrated Nb_2O_5 from Nb_2O_5. [12]. Nb_2O_5 was dissolved in HF to form $[NbOF_5]^{2-}$ or $[NbF_7]^{2-}$ complex. A freshly prepared aqueous solution of ammonium oxalate was added in excess and then aqueous NH_3 was added drop by drop to get hydrous niobium oxide ($Nb_2O_5.nH_2O$) as precipitated. (The flow chart of the synthesis of $Nb_2O_5.nH_2O$ is shown in Fig. 3.1). The precipitate of hydrous oxide was filtered and washed with 10% aqueous NH_3 solution by centrifugation to make the solution fluoride free hydrated Nb_2O_5. In the second step, the stoichiometry amount of hydrated Nb_2O_5 was dissolved in the aqueous solution of citric acid (2mol/mol of niobium ion) with the addition of catalytic amount of hydrogen peroxide, to get clear yellow coloured peroxo-citro-niobate. The addition of H_2O_2 promoted the solubility of the hydrated niobiate in citric acid and also shortened the required dissolution time. The clear solution of peroxo-citro-niobiate was mixed with stoichiometric amount of chromium nitrate (mole ratio of Cr/Nb = 1:1) with constant stirring. The pH of the final solution mixture was adjusted to 7 by addition of aqueous NH_3. This mixture was heated at about 200 ^oC to get a dried black fluffy mass. This dried mass was calcined at 800 ^oC for 2 h to get $CrNbO_4$ nanopowder. The resultant product was collected and subjected into both physical characterization and gas sensor studies. The flow chart of the synthesis of Chromium niobate ($CrNbO_4$) nano powder as shown in Fig. 3.3.

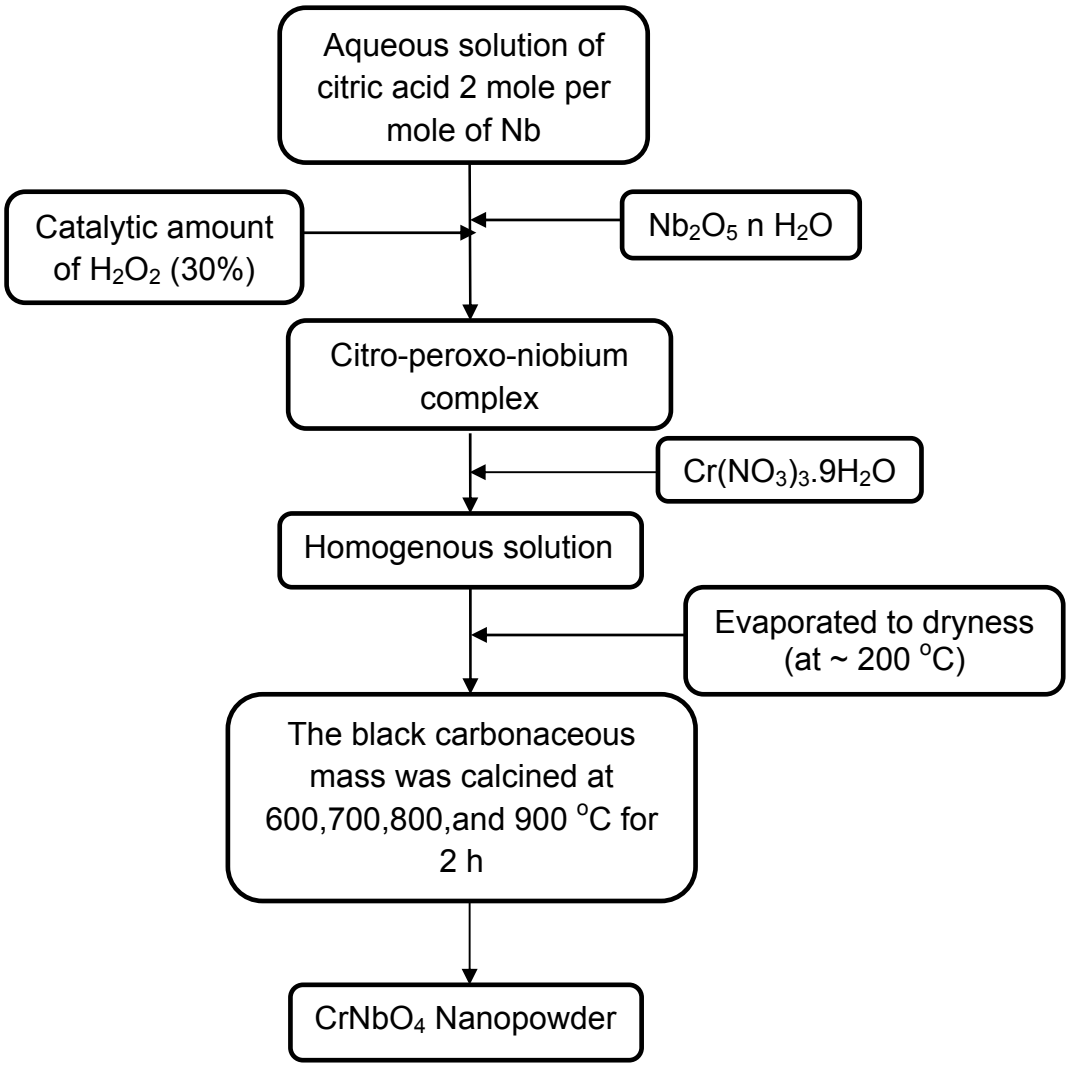

Fig. 3.3. Flow chart for preparation of $CrNbO_4$ Nanopowder by niobium-citrate complex process

3.4. Synthesis of $AlNbO_4$ nanopowder

$AlNbO_4$ nanopowder was obtained by low temperature niobium citrate complex process using following two steps. The first step was the preparation of hydrated Nb_2O_5 from Nb_2O_5. [12]. Nb_2O_5 was dissolved in HF to form $[NbOF_5]^{2-}$ or $[NbF_7]^{2-}$ complex. A freshly prepared aqueous solution of ammonium oxalate was added in excess and then aqueous NH_3 was added drop by drop to get hydrous niobium oxide ($Nb_2O_5.nH_2O$) as precipitated. (The flow chart of the synthesis of $Nb_2O_5.nH_2O$ is shown in Fig. 3.1). The precipitate of hydrous oxide was filtered and washed with 10% aqueous NH_3 solution by centrifugation to make the solution fluoride free hydrated Nb_2O_5. In the second step, the stoichiometry amount of hydrated Nb_2O_5 was dissolved in the aqueous solution of citric acid (2mol/mol of niobium ion) with the addition of catalytic amount of hydrogen peroxide, to get clear yellow coloured peroxo-citro-niobate. The addition of H_2O_2 promoted the solubility of the hydrated niobiate in citric acid and also shortened the required dissolution time. The clear solution of peroxo-citro-niobiate was mixed with stoichiometric amount of aluminium nitrate (mole ratio of Al/Nb = 1:1) with constant stirring. The pH of the final solution mixture was adjusted to 7 by addition of aqueous NH_3. This mixture was heated at about 200 ^oC to get a dried black fluffy mass. This dried mass was calcined at 900 ^oC for 2 h to get $AlNbO_4$ nanopowder. The resultant product was collected and subjected into both physical characterization and gas sensor studies. The flow chart of the synthesis of aluminium niobate ($AlNbO_4$) nano powder is shown in Fig. 3.4.

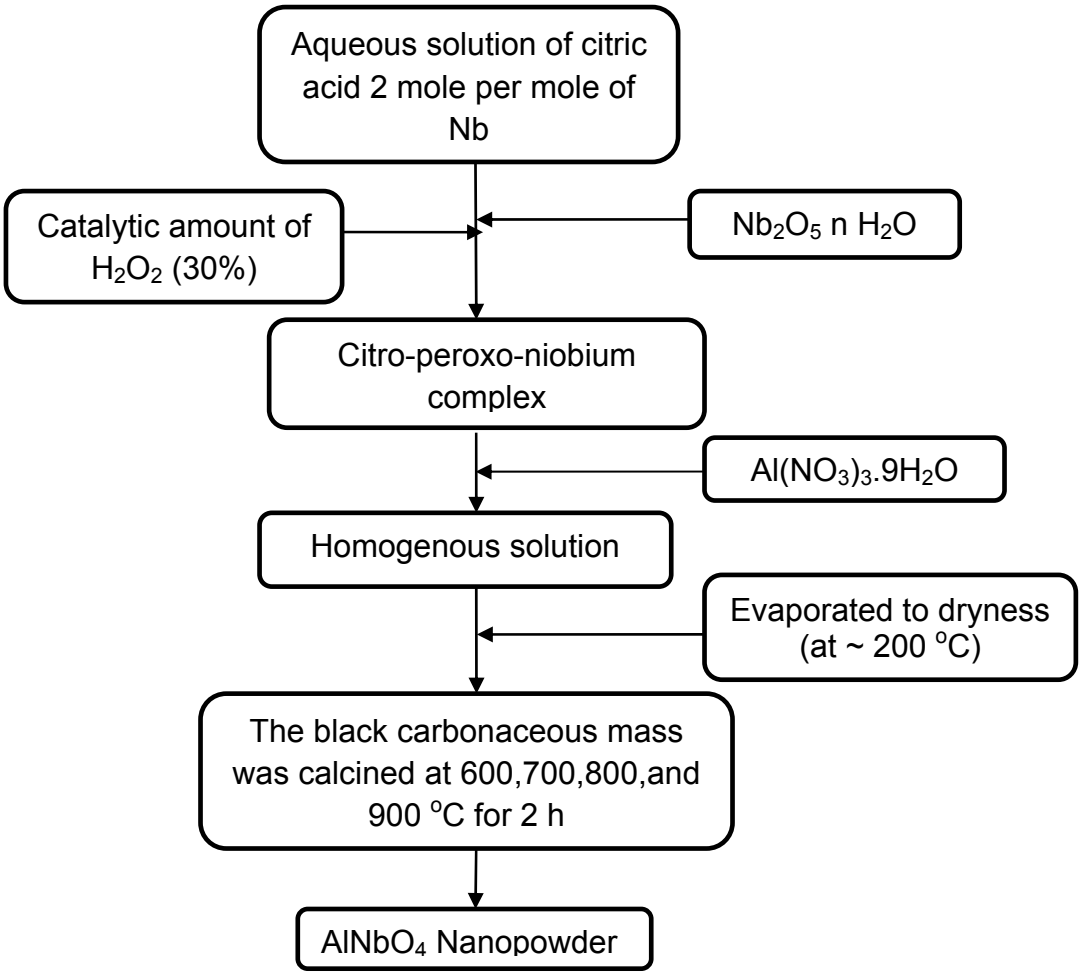

Fig. 3.4. Flow chart for preparation of $AlNbO_4$ nanopowder by niobium-citrate complex process

3.5. Synthesis of $LaNbO_4$ nanopowder

$LaNbO_4$ nanopowder was obtained by low temperature niobium citrate complex process using following two steps. The first step was the preparation of hydrated Nb_2O_5 from Nb_2O_5. [12]. Nb_2O_5 was dissolved in HF to form $[NbOF_5]^{2-}$ or $[NbF_7]^{2-}$ complex. A freshly prepared aqueous solution of ammonium oxalate was added in excess and then aqueous NH_3 was added drop by drop to get hydrous niobium oxide ($Nb_2O_5.nH_2O$) as precipitated. (The flow chart of the synthesis of $Nb_2O_5.nH_2O$ is shown in Fig. 3.1). The precipitate of hydrous oxide was filtered and washed with 10% aqueous NH_3 solution by centrifugation to make the solution fluoride free hydrated Nb_2O_5. In the second step, the stoichiometry amount of hydrated Nb_2O_5 was dissolved in the aqueous solution of citric acid (2mol/mol of niobium ion) with the addition of catalytic amount of hydrogen peroxide, to get clear yellow coloured peroxo-citro-niobate. The addition of H_2O_2 promoted the solubility of the hydrated niobiate in citric acid and also shortened the required dissolution time. The clear solution of peroxo-citro-niobiate was mixed with stoichiometric amount of lanthanum nitrate (mole ratio of La/Nb = 1:1) with constant stirring. The pH of the final solution mixture was adjusted to 7 by addition of aqueous NH_3. This mixture was heated at about 200 ^oC to get a dried black fluffy mass. This dried mass was calcined at 900 ^oC for 2 h to get $LaNbO_4$ nanopowder. The resultant product was collected and subjected into both physical characterization and gas sensor studies. The flow chart of the synthesis of lanthanum niobate ($LaNbO_4$) nano powder is shown in Fig. 3.5.

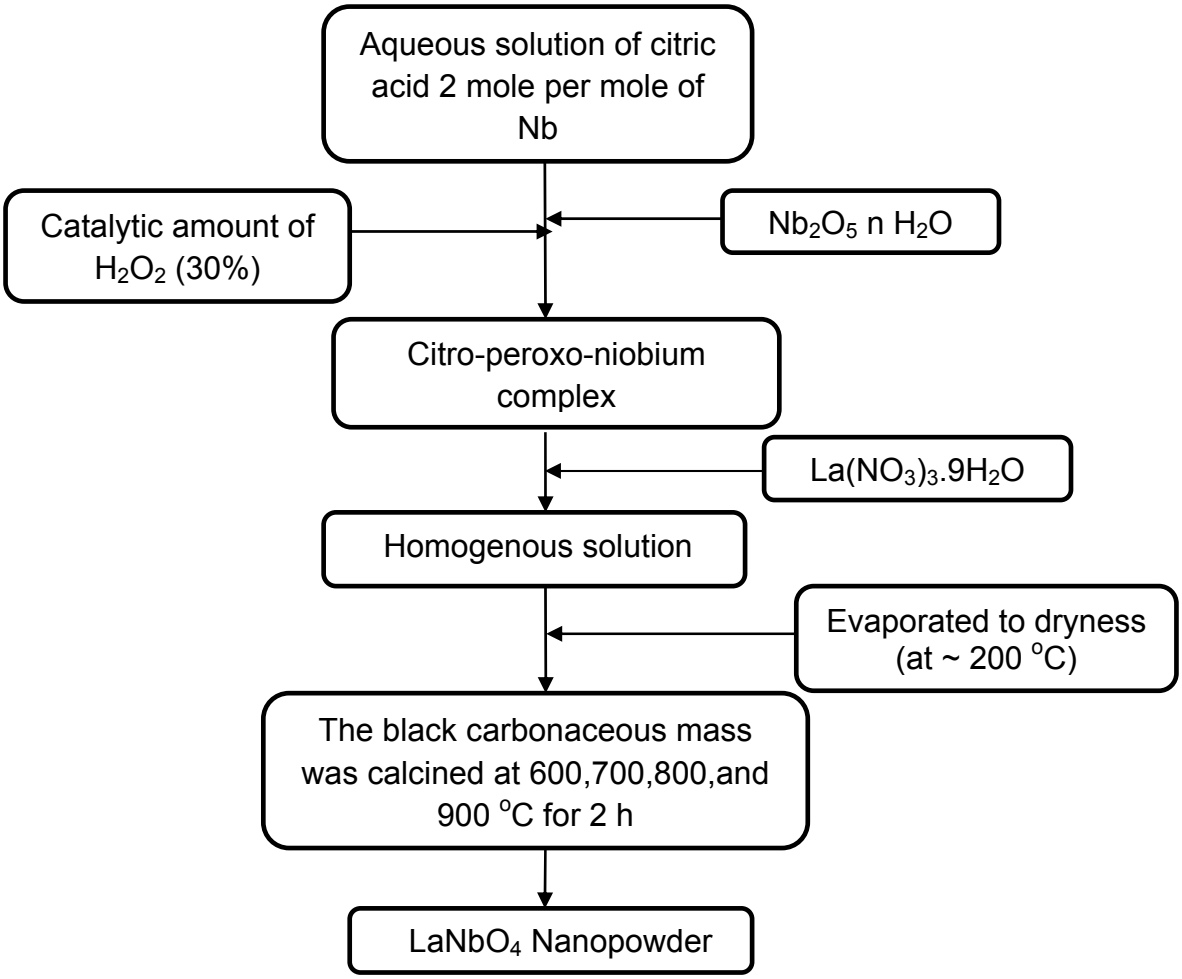

Fig. 3.5. Flow chart for preparation of $LaNbO_4$ nanopowder by niobium-citrate complex process

3.6. Synthesis of $FeNbO_4$ nanopowder

$FeNbO_4$ nanopowder was obtained by low temperature niobium citrate complex process using following two steps. The first step was the preparation of hydrated Nb_2O_5 from Nb_2O_5. [12]. Nb_2O_5 was dissolved in HF to form $[NbOF_5]^{2-}$ or $[NbF_7]^{2-}$ complex. A freshly prepared aqueous solution of ammonium oxalate was added in excess and then aqueous NH_3 was added drop by drop to get hydrous niobium oxide ($Nb_2O_5.nH_2O$) as precipitated. (The flow chart of the synthesis of $Nb_2O_5.nH_2O$ is shown in Fig. 3.1). The precipitate of hydrous oxide was filtered and washed with 10% aqueous NH_3 solution by centrifugation to make the solution fluoride free hydrated Nb_2O_5. In the second step, the stoichiometry amount of hydrated Nb_2O_5 was dissolved in the aqueous solution of citric acid (2mol/mol of niobium ion) with the addition of catalytic amount of hydrogen peroxide, to get clear yellow coloured peroxo-citro-niobate. The addition of H_2O_2 promoted the solubility of the hydrated niobiate in citric acid and also shortened the required dissolution time. The clear solution of peroxo-citro-niobiate was mixed with stoichiometric amount of iron nitrate (mole ratio of Fe/Nb = 1:1) with constant stirring. The pH of the final solution mixture was adjusted to 7 by addition of aqueous NH_3. This mixture was heated at about 200 ^oC to get a dried black fluffy mass. This dried mass was calcined at 800 ^oC for 1 h to get $FeNbO_4$ nanopowder. The resultant product was collected and subjected into both physical characterization and gas sensor studies. The flow chart of the synthesis of iron niobate ($FeNbO_4$) nano powder as shown in Fig. 3.6.

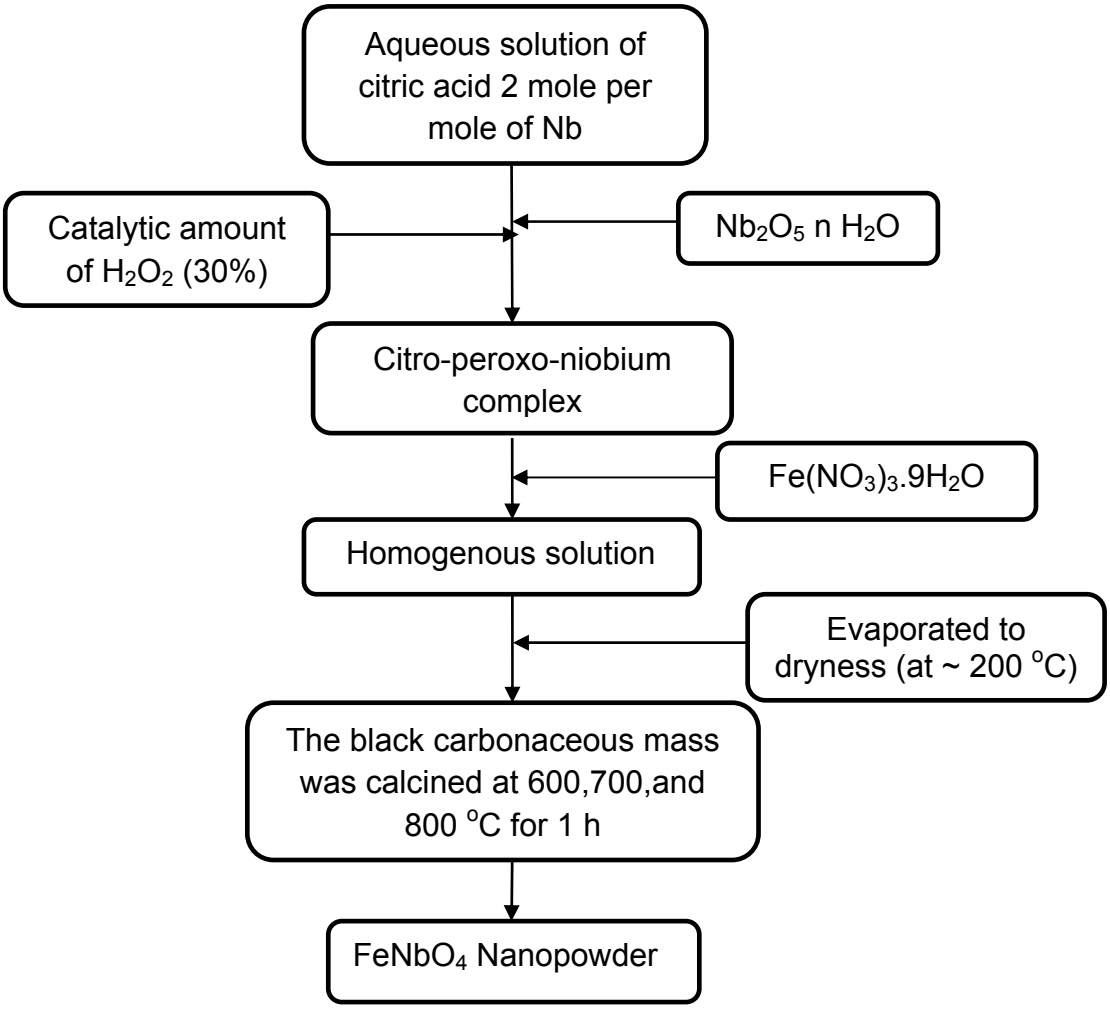

Fig. 3.6. Flow chart for preparation of $FeNbO_4$ nanopowder by niobium-citrate complex process

3.7. PHYSICAL CHARACTERIZATIONS

In a first part, an overview of the most commonly used spectroscopic techniques such as X-Ray Diffraction (XRD), Scanning Electron Microscopy (SEM), Transmission Electron Microscopy (TEM), Diffuse Reflectance spectra (DRS), Electron Dispersive X-ray Spectroscopy, Impedance Spectroscopy, is presented. (Table 3.1).

Table.3.1. Characterization techniques and their information.

Technique	Information
TGA / DTA	Phase formation and/or complete crystallization temperature etc.,
XRD	Phase analysis, crystallinity
SEM	Surface morphology
TEM	Particle size and microstructure
EDX	Composition
DRS	Band gap determination
BET	Specific surface area
Impedance	Conductivity

3.7.1. THERMOGRAVIMETRIC STUDIES

The term thermal analysis refers to a group of techniques in which some physical or chemical properties of a system are measured as a function of temperature. All materials undergo change in their physical and /or chemical properties with temperature. The changes can be detected by suitable transducers which convert the changes into electrical signals which are collected and analyzed to give ’thermograms’ showing the property changes as a function of temperature.

Thermogravimetric analysis (TGA) is an analytical technique used to demine the materials thermal stability and its fraction of volatile components by monitoring the weight change that occurs as a specimen is heated. The measurement is normally carried out in air or in inert atmosphere, such as Helium or Argon, and the weight is recorded as a function of increasing temperature. Sometimes, the measurement is performed in oxygen atmosphere (1 to 5% O_2 in N_2 or He) to slow down oxidation. The results usually appear as a continuous chart record; a schematic, typical, single step decomposition reaction is shown in Fig. 3.7. The sample, usually a few milligrams in weight, is heated at a constant rate, typically in the range of 1 to 20 $Kmin^{-1}$, and has a constant weight W_i, until it begins to decompose at temperature T_i. Under conditions of dynamic heating, decomposition usually takes over a range of temperatures, T_i to T_f, and a second constant weight plateau is then observed above T_f, which corresponds to the weight of the residue W_f and W_i. The difference in weight ΔW is a fundamental property of the sample and is used for quantitative calculation of compositional changes etc. By contrast, the temperature, T_i and T_f depend on variables such as heating rate, nature of the sample (e.g. its particle size) and atmosphere above the sample.

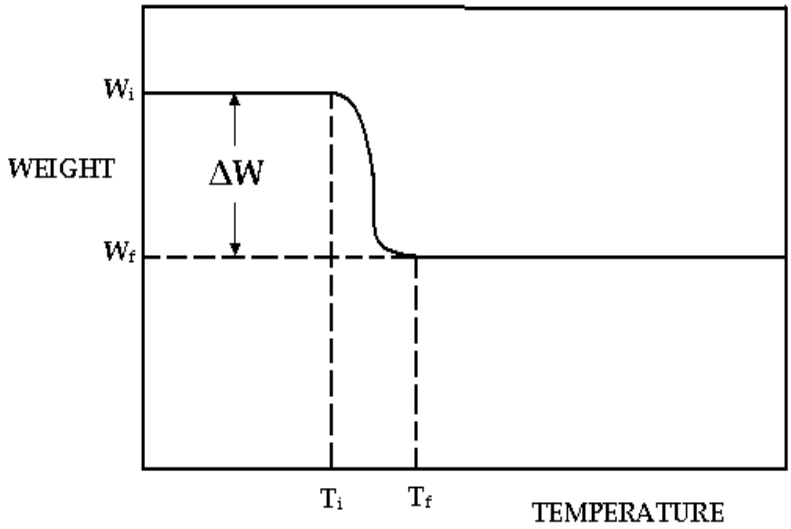

Fig.3.7. Schematic thermogram for a single step decomposition reaction

3.7.2. DIFFERENTIAL THERMAL ANALYSIS

Differential thermal analysis is one in which heat effects associated with chemical and physical changes of a substance, is monitored. In differential thermal analysis is the technique in which the temperature difference between the sample and a thermally inert reference substance is continuously recorded as a function of furnace temperature or time. The measurement of changes in heat content is carried out by heating the two materials at elevated temperatures or cooling to subnormal temperature at a predetermined rate. The thermal effects may either be endothermic or exothermic and are caused by physical phenomena such, as fusion, crystalline structure inversions, boiling, vaporization, sublimation and others. Some enthalpic effects are also caused by chemical reactions. Such as dissociation or decomposition, oxidation, dehydration, reduction, combination, displacement ect. In this way endo and exothermal bands and peaks appearing on the thermograms give information regarding the detection of enthalpic changes. It has been found that most of the above transitions or reactions

produce endothermic heat effects. Only a few, such as oxidation, some decomposition reactions, certain crystalline inversion reactions give exothermic heat effects.

The principle of differential thermal analysis is based on the fact that the thermal effects associated with the physical and chemical changes described above are measured by a differential method in which the sample temperature is continuously compared against the temperature of the thermally inert reference material.This difference in temperature, called differential temperature, ΔT, is recorded as a function of reference material temperature (or furnace temperature) or time, assuming that the furnace temperature rise in linear with time.

In a typical experiment, a furnace is used which contains a sample holder or sample block, the latter of which has two identical and symmetrically located chambers. One set of thermocouple junctions is inserted into the inert material, such as aluminium oxide and the other set of thermo couple junction is placed in the other chamber containing the sample. Some other temperature detecting devices, which have also been employed, are themistor, resistance thermometer or thermopile. The furnace and sample block temperature are then increased at a linear rate, and the temperature difference between the sample and reference material is continuously measured or recorded against the furnace or reference material temperature.

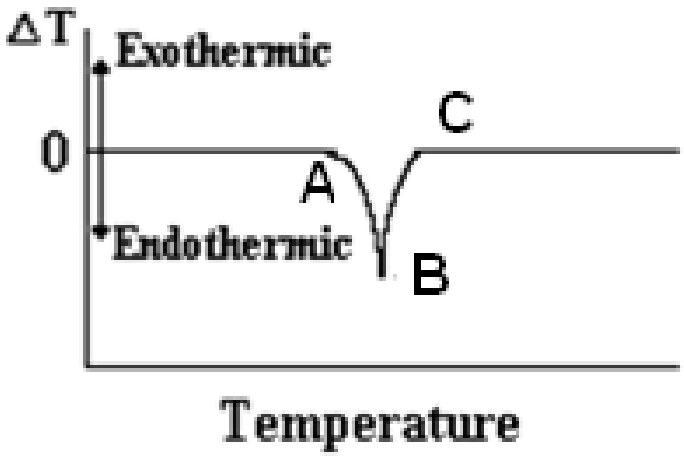

Fig.3.8. The Differential thermal analysis cure

If the sample temperature and differential temperature are compared with each other as a function of time, then a curve of the type shown in (Fig.3.8) is obtained. At point A, it has been assumed that the sample undergoes some type of an endothermic reaction. It is also evident from the sample temperature curve that the sample temperature is no longer linear with respect to time, but lags the furnace temperature as a result of absorption of heat. The reaction becomes complete at B and the sample temperature increases and after sometime it becomes equal to the furnace temperature again at C. During the actual transition which begins at A the sample and reference material temperature differ ideally in the case of differential temperature curve. A peak ABC, with maximum at B is thus obtained in the curve. Beyond B, the curve returns to the base line $\Delta T = 0$ due to equalization of sample and reference temperatures. Although only an endothermic transition is illustrated here, the curve deviations would be in an opposite inverted position for an exothermic transition. Hence each substance will, in general, give a curve whose number, shape and position of various endothermic and exothermic peaks act as a means of qualitative identification of the substance. The

technique can also be used to evaluate quantitatively the amount of substance present by making use of the fact that the reaction is proportional to the amount of reacting substance. It is also interesting to note that thermogravimeteric analysis and differential thermal analysis are complementary techniques, because the information obtained by the application of the one approach is often enhanced by the application of the other method.

In the present work, the phase formation and/or complete crystallization temperature of the prepared sample was characterized with simultaneously recorded thermogravimeteric (TGA) and differential thermal analysis (DTA) at heating rate of 10 ^{o}C/min using Pyris Diamond TG/ DTA as shown in Fig.3.9.

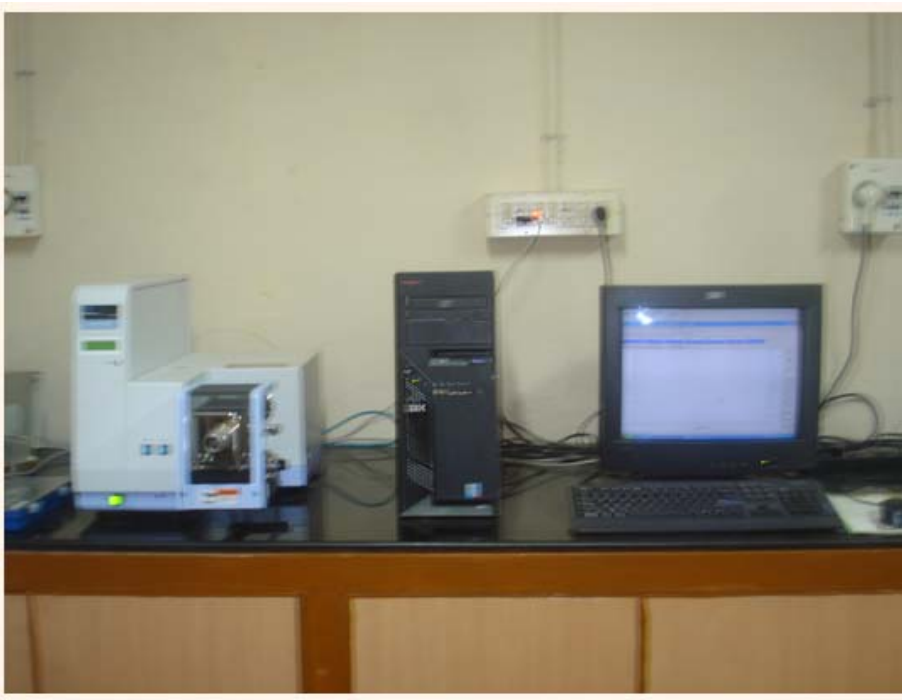

Fig.3.9. Photograph of thermal analysis system

3.7.3. X-Ray Diffraction studies

This technique analyzes the interaction of X-rays with the crystalline matter through their diffraction. The X-ray beam diffracts when crossing the crystal and produces beams at different angles depending on the X-ray wavelength, the crystal orientation and the structure of the crystal. The common X-rays wavelengths used are Mo- Kα at 0.71359 Å and the Cu Kα at 1.54056 Å.

X-ray spectra allow us to identify and analyze any crystalline matter. X-ray region is a part of electromagnetic spectrum ranging between 0.1 to100 A° (equivalent to an energy of 0.1 – 100 KeV). The breaking of X-rays into dark and bright bands caused by the interference of one part of the beam with another when the ray is deflected by an opaque object with accompanying variation in the intensity of X-rays in different directions is called X-ray diffraction. X-ray diffraction method is one of the most important tools applied in solid-state chemistry, as it constitutes a powerful and readily available method for determining atomic arrangements in materials.

The application of XRD technique to polycrystalline materials such as semiconductor nanopowders gives us a set of peaks with angular separations satisfying the Bragg's law. Structure identification and the determination of lattice parameter are obtained from the X-ray diffraction pattern using Bragg's law;

$$2d\sin\theta = n\lambda$$

where, "d" is the inter planar distance of the material can be calculated from the equation. The "d" spacing is varied by the crystal assembly and the intensities of the

diffracted rays depend upon the crystal size of the material. By using Scherer's equation, one can calculate the crystallites size.

$$D = 0.9\lambda / \beta \cos\theta$$

where, λ the wavelength of the monochromatic X-ray radiation θ is the Bragg angle and β is the breadth of the diffraction peak at full width half maximum of X-ray diffraction peak. The crystalline peaks observed in the X-ray diffraction patterns are indexed by assigning Miller indices namely (hkl) using standard analytical methods.

In X-ray diffraction studies, a monochromatic X-radiation such as K_α radiation (1.54 Å) is used. This is obtained from X-ray tube using copper as the target. As nickel strongly absorbs K_β (1.39 Å) radiation, monochromatic K_α radiation can be obtained by using a nickel foil as filter. The powder X-ray diffraction method involves the diffraction of a collimated monochromatic beam from a powder sample containing an enormous number of tiny crystals having random orientation. The diffracted beam from the sample passes through the receiving slit and enters the Geiger counter. A chart recording the amplified output of the Geiger counter gives directly a plot of intensity versus scattering angle (2θ).

The diffraction of X-rays is a good tool to study the nature of the crystalline substances. In crystals, the ions or molecules are arranged in well-defined positions in planes in three dimensions. The impinging X-rays are reflected by each crystal plane. Since the spacing between the atoms and hence the planes can't be same or identical for any two chemical substances, this technique provides vital information regarding the

arrangement of atoms and the spacing in between them and also to find out the chemical compositions of crystalline substances. The sample under study can be of either a thin layer of crystal or in a powder form. Since, the power of a diffracted beam is dependent on the quantity of the corresponding crystalline substance, it is also possible to carry out quantitative determinations. These peaks can be indexed and related to a determinate crystalline structure using some patron tables as the well-known JCPDS data.

This analytical technique brings an easy quantification of the crystalline phases that compose the samples, and the possibility of evaluating the mean grain size of the polycrystalline samples. However, in order to obtain accurate results in this quantification, we have to be sure of the sample structure, and some initial patron models are needed.

In this study, the phase identification in prepared sample was performed using room temperature X-ray powder diffraction (Model: X' pert-pro diffractometer) with Cu-K_α radiation (λ = 1.5406 Å) and Ni filter (Fig. 3.10). In the XRD studies, the powders obtained at different heat treatment temperatures were mounted in the sample holder and recorded in the 2θ range from 20-80 ^{o}C. The X-ray diffraction lines were analyzed using PCPDFWIN Version 2.4, JCPDS-ICDD (2003). The crystallite size (D) of the compositions was calculated using Scherer's equation to the full widths at half maximum (fwhm).

Fig.3.10. Photograph of X-ray diffractometer

3.7.4. SCANNING ELECTRON MICROSCOPE (SEM) STUDIES

Scanning electron microscopy is used primarily for the study of surface topography of solid materials. Scanning electron microscope permits a depth of field greater than optical or transmission electron microscopy. The resolution of scanning electron microscope is about 3nm, approximately two orders of magnitude greater than the optical microscope and one order of magnitude less than the transmission electron microscope. Thus, the SEM bridges the gap between these two techniques.

An electron beam passing through an evacuated column is focused by electromagnetic lenses onto the specimen surface. The beam is then projected over the specimen in synchronism with the beam of a cathode ray tube (CRT) display screen. The elastically scattered secondary electrons are emitted from the sample surface and collected by a scintillator. In this way, the secondary electrons emitted from the sample are used to form an image on the CRT display screen.

Differences in secondary emission result from the changes in surface topography. If elastically back scattered electrons are collected to form the image, contrast results from the compositional differences. Cameras are provided to record the images on the display screen. The scanning electron microscope permits not only observation of very fine details (high resolution) but also good focus over a wide range of specimen surfaces (large depth of field). If an element of the specimen has a low atomic number, the incident electrons will show a tear-drop shaped diffusion, while if the element has a high atomic number, the incident electrons will show a hemispheric diffusion. Higher accelerating voltages expand the diffusion area much deeper. In the course of diffusion, the incident electrons gradually lose their energy until

absorbed by the specimen (detected as absorbed current). In this process, low energy secondary electrons are reflected outside the specimen, with loosing much of their energy.

In addition, the Auger effect causes Auger elements very near to the specimen surface, when incident electrons collide with constituent atoms of the specimen, most of the electron energy is converted into heat, but a portion of it is consumed to produce X-rays, visible and infrared cathode luminescence together with secondary and Auger electrons. Quanta (Secondary electrons), backscattered electrons, X-rays and so on, carry information which describes the nature of the specimen (its atomic number, elemental distribution, topography, surface potential distribution, magnetic domain, chemical and crystallographic characteristics etc.). This information is converted into a video signal and displayed on a CRT as a scanning image. Depending on the type of detectors used this method is classified in to two as: Energy Dispersive Spectrometry (EDS) and Wavelength Dispersive Spectrometry (WDS). This technique is used extensively in the analysis of metallic and ceramic inclusions, inclusions in polymeric materials, diffusion profiles in electronic components.

In the present study, the surface morphology of the synthesized nanopowders were analyzed by Scanning electron microscope (Model: Hitachi, SN-3400N) as shown in Fig. 3.11.

Fig. 3.11. Photograph of Scanning Electron Microscope

3.7.5. TRANSMISSION ELECTRON MICROSCOPE STUDIES

In this technique, a beam of high-energy electrons (typically 100- 400keV) is collimated by magnetic lenses and allowed to pass through a specimen under high vacuum. The transmitted beam and a number of diffracted beams can form a resultant diffraction pattern, which is imaged on a fluorescent screen kept below the specimen. The diffraction pattern gives the information regarding lattice spacing and symmetry of the structure under consideration. Alternatively, either the transmitted beam or one of the diffracted beams can be made to form a magnified image of the sample on the viewing screen as bright-and darkfield imaging modes respectively, which give information about the size and shape of the micro-structural constituents of the material. High-resolution image, that contains information about the atomic structure of the material, can be obtained by recombining the transmitted beam and diffracted beams together.

In TEM, electron emitted thermionically or as a result of application a high field is used. For conventional electron microscopy, the former are suitable with brightness of the order of 10^3 A $mm^{-2}Sv^{-1}$, where as in high-resolution microscopy, the later are used with a brightness of several orders higher. Electrons are associated with a wavelength depending on their energy. For an accelerating potential of volts, the electron wave length is given in angstroms units by the equation $\lambda = \sqrt{}$ (150/v) . Electron beam energies between 100 & 300 Kev are usually employed. It is immediately clear that wave length can be obtained as a narrow beam and focused. The two options available are: (a) the electrostatic lens and (b) the magnetic lens. The former requires very high field of focus and is technically difficult to perfect. So the magnetic lens is used

predominantly. A magnetic field applied normal to the electron motion will make it assume a circular path. In the electron microscope, the field is almost but not quiet parallel to the beam. The combination of the accelerating voltage and the magnetic field causes a helical path to be traversed. The variation of the current through a magnetic field coil enables one to change a focal length. A TEM can also operate in diffraction mode. By using a monochromatic energetic and very narrow beam of electrons, one can analyze the structure of nano-materials.

In the present study, the particle size and crystalline quality of the synthesized powder were confirmed by transmission electron microscopy (Model: Philips, CM-20) at 200 kV. For TEM investigation, an ultrasound bath was used to disperse the nanopowders in ethanol. A drop of this suspension was evaporated into holey carbon coated copper grid. After evaporation of the ethanol, the remaining particles were viewed in the microscope as shown in Fig. 3.12.

Fig. 3.12. Photograph of Transmission Electron Microscopy

3.7.6. ENERGY-DISPERSIVE X-RAY SPECTROSCOPE STUDIES

To make a quantitative composition analysis, Energy-Dispersive X-ray Spectroscopy technique (EDX) was applied. EDX units were attached to electron microscopes, therefore it was a useful method to determine the elemental composition of the particles being observed under TEM or SEM. Taking the spectrum in different points of the sample, we made a quantitative analysis. The spectrum of Au was used as reference.

This technique allows a rapid evaluation of a specimen, i.e. identification of the elements that are present in a sample. In its simplest form, quantitative analysis proceeds by determining the energies of x-ray emission. At low x-ray energy (less than 3 keV), peak separation and the limited resolution of the EDS spectrometer will likely restrict element identification to only one peak. But at low-energy L or M lines will be accompanied by high-energy K or L lines in the 4-20 keV range, which can aid identification. Below 1 keV, quantitative EDS analysis is difficult. The error is defined as the rate between the Standard deviation.

The main problem in the EDS used was the impossibility of detecting elements behind Na (Z=11). Elements such as B, C, N and O won't be detected. This is due to the use of a Be window to avoid contamination inside the microscope chamber, which only leads to detect elements below Na (Z=11). Thus, in the case of oxides we will just detect its metallic component.

3.7.7. BET SURFACE AREA MEASUREMENT

The surface area of all the synthesized nanopowder was measured using the BET nitrogen adsorption and desorption method (Micrometritics, ASAP 2020) at -196 ^{o}C. The features of the method of analysis are qutlined below in brief. BET theory aims to explain the physical adsorption of gas molecules on a solid surface and serves as the basis for an important analysis technique for the measurement of the specific surface area of a material.

The concept of the theory is an extension of the Langmuir theory, which is a theory for monolayer molecular adsorption, to multilayer adsorption with the following hypotheses: (a) gas molecules physically adsorb on a solid in layers infinitely; (b) there is no interaction between each adsorption layer; and (c) the Langmuir theory can be applied to each layer. The resulting BET equation is expressed by:

$$\frac{1}{v(1 - Po/P)} = \frac{c - 1}{v_m c}\ \frac{P}{Po}\ + \frac{1}{v_m c} \qquad (1)$$

P and P_o are the equilibrium and the saturation pressure of adsorbates at the temperature of adsorption, v is the adsorbed gas quantity (for example, in volume units), and v_m is the monolayer adsorbed gas quantity. c is the BET constant, which is expressed by:

$$c = exp\frac{(E_1 - E_L)}{RT} \qquad (2)$$

E_1 is the heat of adsorption for the first layer, and E_L is that for the second and higher layers and is equal to the heat of liquefaction. Equation (1) is an adsorption isotherm and can be plotted as a straight line with $1 / v[(P_0 / P) - 1]$ on the y axis and $\varphi = P / P_0$ on the xaxis according to experimental results. This graph is called a BET plot. The

linear relationship of this equation is maintained only in the range of $0.05 < P / P0 < 0.35$. The value of the slope A and the yintercept I of the line are used to calculate the monolayer adsorbed gas quantity v_m and the BET constant c. The following equations can be used:

$$vm = \frac{1}{A+1} \tag{3}$$

$$c = 1 + \frac{A}{I} \tag{4}$$

The BET method is widely used in surface science for the calculation of surface areas of solids by physical adsorption of gas molecules. A total surface area S_{total} and a specific surface area S are evaluated by the following equations;

$$S_{BET,Total} = \frac{(v_m N_s)}{V} \tag{5}$$

where v_m is in units of volume which are also the units of the molar volume of the adsorbate gas

$$S_{BET} = \frac{S_{total}}{a} \tag{6}$$

N: Avogadro's number,

s: adsorption cross section of the adsorbing species,

V: molar volume of adsorbate gas

a: mass of adsorbent (in g)

The surface area determination involves admitting an adsorbing gas (nitrogen) to a known weight of the sample. A series of values for V_a (volume of the gas adsorbed) at various pressures (P) have been noted. A plot of W_s versus P_s, where W_s is the weight

of the sample and P_s is the saturation pressure taken at the temperature of the sample during the run, yields an adsorption isotherm. These values substituted in the BET equation along with saturation pressure data, permit the plot P/V ($P-P_s$) versus P/P_s giving a straight line, the intercept and slop of which are $1/V_m^c$ and $C-1/V_m^c$ respectively. The value of V_m is thus readily extracted for a series of measurement. Once the plot is made, the specific surface area of the sample, S_w in m^2/g is calculated using the appropriate area occupied by the single adsorped gas derived from the relationship.

$$Sw = \frac{4.35}{slop + intercept}$$

Accuracy of the calculated surface area of adsorption methods depends on the accuracy of determining the volume of adsorbed gas under monolayer and the knowledge of the cross-sectional area occupied by each adsorbed molecule (e.g., N_2 = 16.2 $Å^2$) In addition, adsorption model assumes that all sites on the particle surface have equal activity. Generally the accuracy of this method is ± 5%. Model BET instrument to determine the surface area as shown in Fig. 3.13.

3.7.8. Diffuse reflectance measurements

Ultraviolet-visible (UV-Vis) adsorption spectra, equipped with a diffuse reflectance measurements (Model: Varian, cary-5000). Based upon the onset of the diffuse reflectance spectra of the powdered materials, the absorption edge and band gap energies of the nanocomposites were determined and compared.

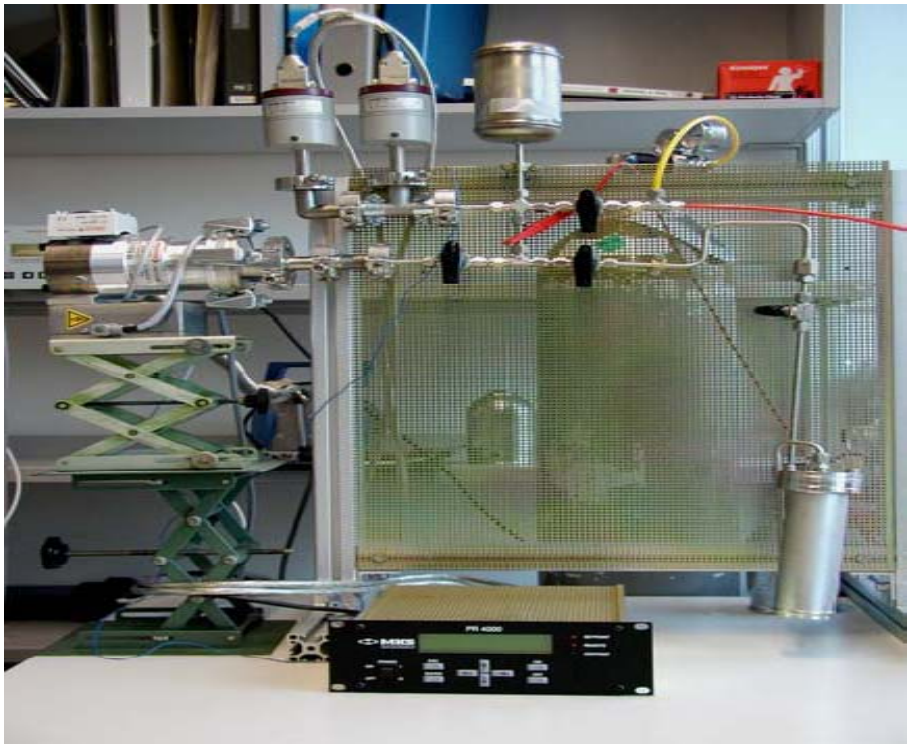

Fig.3.13. BET instrument to determine the surface area

The Praying Mantis DRA is designed to measure diffuse reflectance. Light is projected onto the horizontally positioned sample, and diffuse reflected light is collected by the two large hemispherical mirrors positioned above the sample. This reflected light is then directed toward the instrument detector (Fig.3.14). The Praying Mantis is ideal for the measurement of samples that must be kept horizontal (such as powders, liquids or pastes), as well as very small samples (image at the sample position is only 3 mm in diameter).

The absorption edge or band edge is defined as the transition between the strong short-wavelength and the weak long-wavelength absorption in the spectrum of a solid, generally a semiconductor. The spectral position of this edge is determined by the energy separation between the valence and conduction bands of the material in question. In the case of transparent solids, the absorption edge can be measured using transmittance techniques. Diffuse reflectance measurements provide a more appropriate means of measurement for powdered materials. Using a Cary 500 spectrophotometer equipped with a Praying Mantis diffuse reflectance accessory, ultraviolet-visible (UV-Vis) diffuse reflectance spectra of novel nanocomposite materials have been acquired. Based upon these diffuse reflectance spectra of the powdered materials, absorption edge have been calculated.

The present study aimed to directly measure the absorption edge and band-gap energies of prepared nanostructured materials, based on the onset of UV-Vis diffuse reflectance spectra in the wave length range of 100-1000 nm.

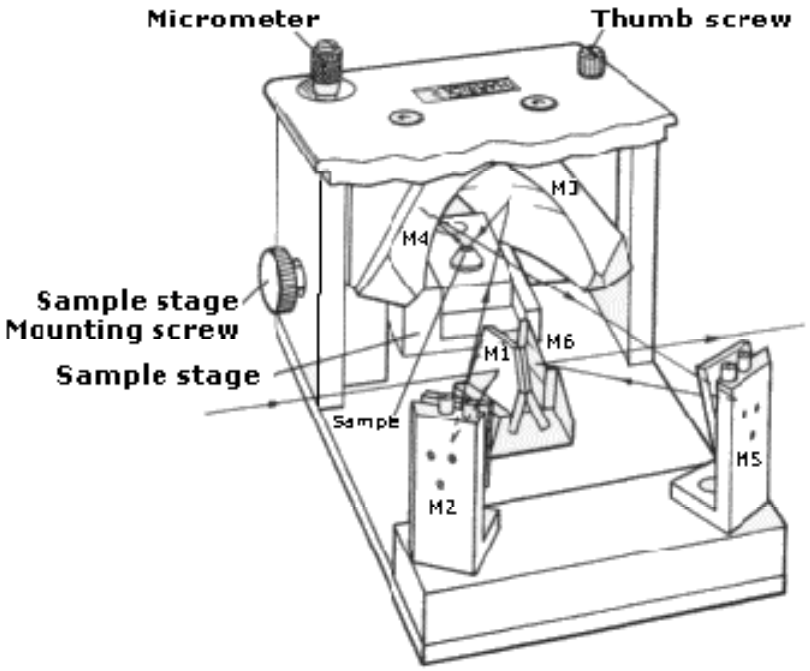

Fig.3.14. diffuse reflectance accessory optical diagram

3.7.9. IMPEDANCE ANALYSIS

Electrochemical impedance spectroscopy is an excellent tool to characterize many of the electrical properties of materials and their interfaces with the electronically conducting electrodes. Electrical conductivity of polymer electrolytes is usually measured using a cell with the configuration of electrode/test sample. The electrochemical behaviour of electrode and/or electrolyte materials is usually made with cells having two identical electrodes applied to the faces of a sample in the form of a circular cylinder or rectangular parallelepiped. However, if devices such as chemical sensors or living cells are investigated, this simple symmetrical geometry is often not feasible. Vacuum, a neutral atmosphere such as argon, or oxidizing atmosphere is variously used. Thus, impedance behaviour is dependent on frequency and is therefore obtained from a.c. measurements over a wide range of frequencies.

The concept of electrical impedance was first introduced by Oliver Heaviside in the 1880's and was soon after developed in terms of vector diagrams and complex representation by A. E. Kennelly and especially C. P. Steinmetz. Impedance is a more general concept than resistance because it takes phase differences into account, and it has become a fundamental and essential concept in electrical engineering. Impedance spectroscopy is thus just a specific branch of the tree of electrical measurements. The magnitude and direction of a planar vector in a right hand orthogonal system of axes can be expressed by the vector sum of the components *a* and *b* along the axes, that is, by the complex number $Z = a + jb$. The imaginary number $j \equiv \sqrt{-1} \equiv \exp(j\pi\sqrt{/2})$ indicates an anticlockwise rotation by π/2 relative to the *x* axis. Thus, the real part of *Z*, *a*, is in the direction of the real axis *x*, and the imaginary part *b* is along the *y* axis. An impedance

$Z(\omega) = Z' + jZ''$ is such a vector quantity and may be plotted in the plane with either rectangular or polar coordinates, as shown in Fig. 3.15. Here the two rectangular coordinate values are clearly

$$\text{Re}\,(Z) \equiv Z' = |Z|\cos(\theta) \text{ and } \text{Im}\,(Z) \equiv Z'' = |Z|\sin(\theta)$$

with the phase angle

$$\theta = \tan^{-1}(Z''/Z')$$

and the modulus

$$|Z| = [(Z') + (Z'')]^{1/2}$$

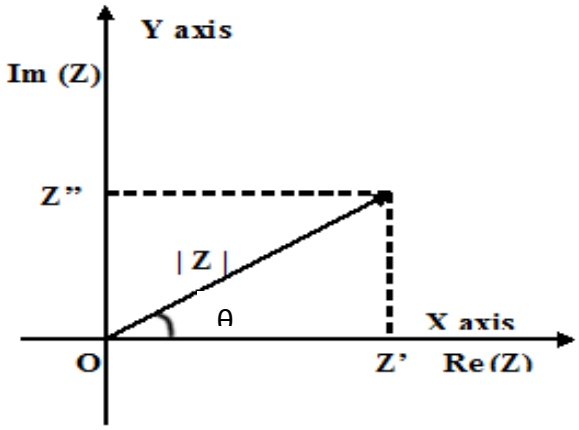

Fig 3.15. The impedance *Z* plotted as a planar vector using rectangular and polar coordinates

This defines the Argand diagram or complex plane, widely used in both mathematics and electrical engineering. In polar form, Z may now be written as $Z(\omega) = |Z| \exp(\theta)$, which may be converted to rectangular form through the use of the Euler relation $\exp(j\theta) = \cos(\theta) + j \sin(\theta)$. It will be noticed that the original time variations of the applied voltage and the resulting current have disappeared, and the impedance is time-invariant (provided the system itself is time-invariant). In general, Z is frequency-dependent, as defined above. Conventional Impedance spectroscopy consists of the (nowadays often automated) measurement of Z as a function of n or ω over a wide frequency range. It is from the resulting structure of the $Z(\omega)$ vs. ω response that one derives information about the electrical properties of the full electrode/electrolyte material systems. In general, in test cells involving polymeric electrolytes it is often possible to ignore the inductive components and to represent the data in the form of a plot of real (X-axis) against imaginary (Y-axis), where the real contributions arise from the resistance and the imaginary terms from the capacitances and its corresponding plot with equivalent circuit as shown in Fig. 3.16. It is explained that the plot consisting of a semi-circle followed by a spike in terms of simple equivalent circuit and the electrolyte resistance can be obtained by extrapolating the spike to the point of intersection with the x-axis.

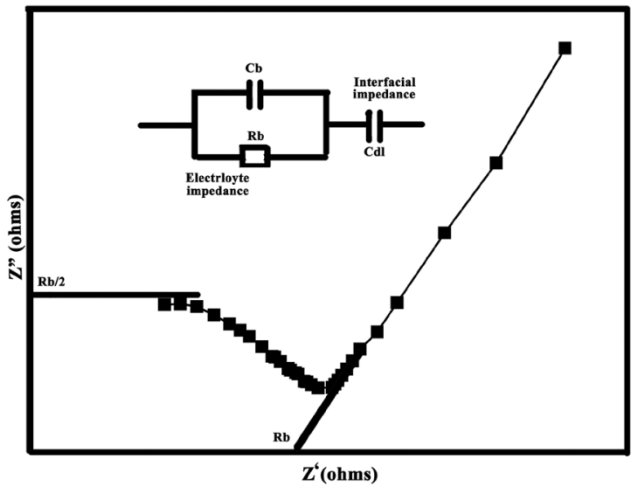

Fig.3.16. Schematic representation of complex impedance plot

In addition, impedance spectroscopy is a relatively new and powerful method of characterizing many of the electrical properties of materials and their interfaces with electronically conducting electrodes. It may be used to investigate the dynamics of bound or mobile charge in the bulk or interfacial regions of any kind of solid or liquid material: ionic, semiconducting, mixed electronic–ionic and even insulators (dielectrics).

Electrical Conductivity Set Up

The essential parts of the conductivity cell arrangements are

- A cell to hold the thin film.
- A heating furnace.
- A thermocouple.
- A temperature controller/ programmer.

Cell Design

In the present study, the bulk conductivity as a function of composition and temperature is evaluated from complex impedance plots. The conductivity cell diagram as shown in Fig. 3.17.

The cell consisted of two stainless rods of 1 cm diameter and 30 cm length gas-welded on the two top edges of the inner hole of the rigid block. Of these, one rod was used as a current carrying lead. A rod of 30 cm length and 1 cm diameter was used as a second electrode. The second electrode was held through a spring load arrangement so as to keep the sample under an optimum stress condition and to ensure good electrical contact between the sample film and the electrodes. A flat portion of 20 mm diameter had been welded at one end of the rods, which serves as blocking electrodes for ions. The upper portion of the current carrying electrodes was held in place with a circular Teflon lid. A small hole was made on one side of the stainless steel block at the area exactly where the sample would be placed for measurement. A chromel-alumel thermocouple was used for measurement. Care was taken to place the tip of the thermocouple close to the film to measure as accurately as possible the temperature of the sample environment. The thermocouple was connected to temperature controller-cum-programmer for controlling the sample temperature within ±1ºC. During the conductivity measurement the sample was kept in a vacuum chamber (using continuous pumping) to avoid contact of the sample with the atmosphere. In the present study, electrical conductivity measurements were carried out on the prepared nanopowder using computer controlled Potentiostat /Galvanostat (Model: Micro auto lab type III) in the frequency range of 1Hz-500 KHz at 30-175 °C.

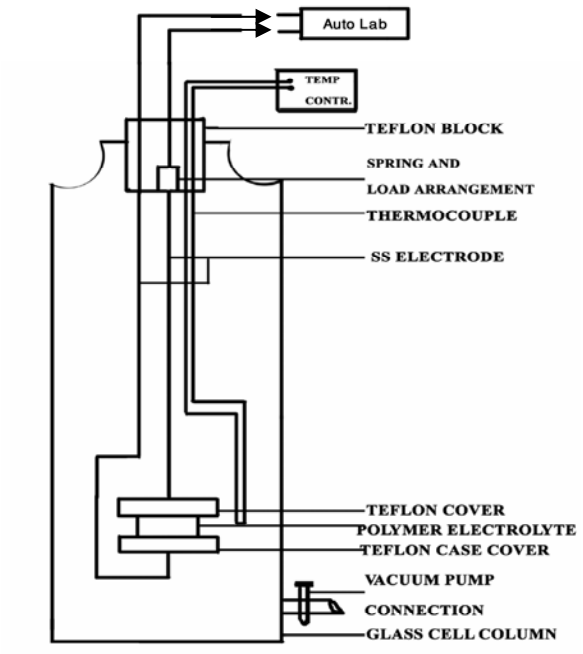

Fig. 3.17. Schematic representation of conductivity cell diagram

The graph was drawn between Z' ohms and Z" ohms using graphical software name called Origin. From the graph, the value of bulk resistance, R_b was found. The electrical conductivity was calculated using the formula;

$$\sigma = l / R_b A$$

where σ – conductivity, l – thickness of the sample, R_b – resistance of the sample, A – area of the sample. Arrhenius relation generally describes the electrical conductivity versus temperature behaviour in material

$$\sigma = \sigma_0 \exp(-Ea/kT)$$

where σ_0 – a constant, Ea – activation energy, k – Boltzmann constant, T- absolute temperature (K).

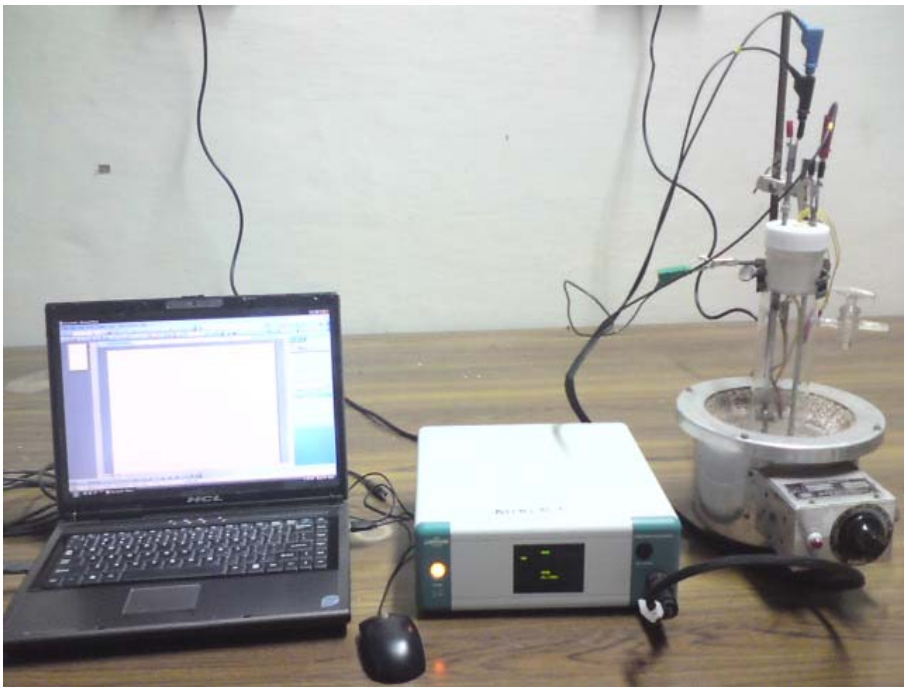

Fig. 3.18. Photograph of Potentiostat /Galvanostat (Model: Micro auto lab type III) for electrical conductivity measurement

3.8. SENSOR STUDIES

For gas-sensing properties, the prepared Niobate based nanopowders were grounded into fine powders, and then mixed with 2% poly vinyl alcohol as a binder to form a paste. The pastes were, respectively, coated onto alumina tube substrates provided with platinum wire electrodes for electrical contacts. The thickness of sensing layer was kept ~30 μm for each powder. The alumina tube was about 8 mm in length, 2 mm in external diameter and 1.6 mm in internal diameter. Then the sensor element was annealed at 500 ^{o}C for 1 h, to make it rigid and impart its porous properties. The static gas-sensing unit was used to examine the sensing performance of the sensors. The response of the sensors was studied in a sealed test chamber (300 cm^3) made of aluminum with a gas inlet and an outlet. The sensor element, with a nichrome heater to provide the required temperature and a chromel–alumel thermocouple (TC) for indicating the operating temperature was fixed inside the test chamber to study the gas-sensing characteristics. The schematic of sensor element used for the gas sensitivity studies as shown in Fig. 3.19. The concentrations of the test gases were obtained by diluting them with fresh air. The test gas was injected into the test chamber through an injection port and the electrical resistance was measured as a function of time till it attained constant value. The chamber was then purged with air and the experiments were repeated. The electrical resistance of the sensor element was measured by means of conventional circuitry in which the load resistor was connected in series with the sensor element. The voltage drop across the sensor element, at a circuit voltage of 10 V, was used to calculate its electrical resistance of the test gases. The electronic circuit used as shown in Fig. 3.20. The electrical resistance was measured both in the

presence and absence of a test gases. The sensor response (S) was calculated using the following equation.

$$S = \frac{\Delta R}{R_a} = \frac{(R_a - R_g)}{R_a}$$

where ΔR is the change of resistance of the sensor under a given test gas (R_g) at constant temperature and base resistance at constant temperature under test gas free atmosphere (R_a). In this study, the gas sensing properties of gases such as LPG, C_2H_5OH and NH_3 were measured at 50 to 350 ^oC. At the optimum operating temperature, the sensor response was measured as a function of various concentrations of test gases as well as with time.

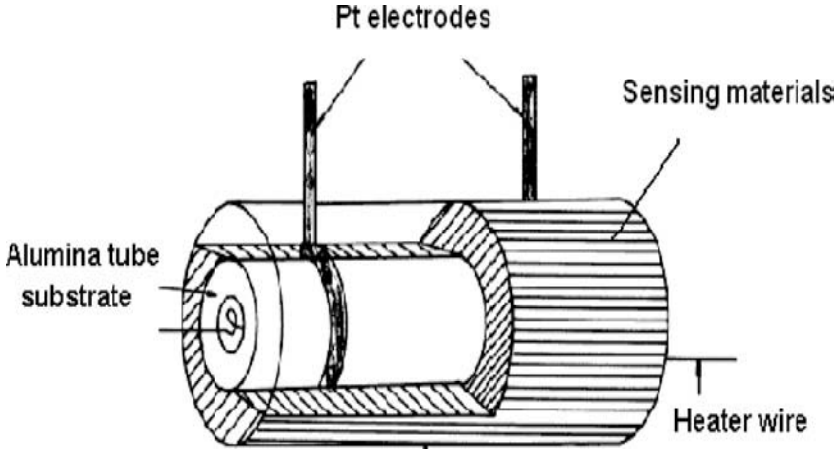

Fig. 3.19. Sensor element used for gas sensitivity studies

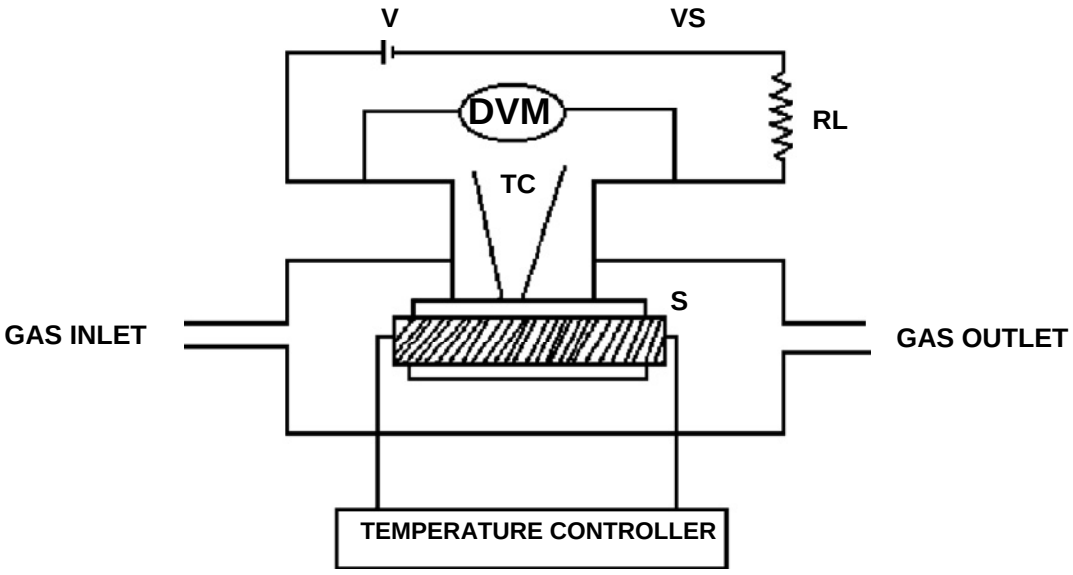

Fig. 3.20. Electric circuit for gas sensor

TC- Thermocouple, S – Sensor element, RL – Standard resistance

VS – Voltage drop across sensor, V – Supply Voltage

Fig. 3.21. The photograph of sensor analysis set-up

REFERENCES

1. W.Wesley and M.Wendlandt, Thermal analysis, John Wiley NewYork,1964.
2. B.K. Sharma, Instrumental Methods of Chemical Analysis, (1994).
3. Instruction Manual for Quansorb Surface area Analyzer, Quanta Chrome Corporation, NY,USA.
4. Perkampus, H.-H., 'Encyclopedia of Spectroscopy', VCH, 1995.
5. Cheng Peng Zhen Zhang. Ceramics International, 33(2007)1133.
6. Chyi-Ching Hwang, Tsung-Yung Wu, Jun Wan, Jih-Sheng Tsai, Mater.Sci. Eng., B, 111(2004)49.
7. P.J. Goodhew and F.J. Humphreys, Electron microscopy and analysis, Second Edition, Taylor and Francis, London.
8. M.D. Shaji Kumar, T.M. Srinivasan, P. Ramasamy, C. Subramanian, Mater, Lett., 25(1994)171.
9. S. Richard Prabhu Gnanakan, Ph.D thesis, Alagappa University, May – 2009.
10. TichLam Nguyena, and Andrew R. Hind. Varian, Australia.
11. N.T. Kalyana Sundaram, T. Vasudevan, A. Subramania, J. Phys.Chem. Solids, 68 (2007)264.
12. J. Rose Mac Donald (Ed.), Impedance Spectroscopy, John Wiley, New York, (1987).
13. M.D. Shaji Kumar, T.M. Srinivasan, P. Ramasamy, C. Subramanian, Mater, Lett., 25 (1994)171.
14. A.V. Kadu, S.V. Jagtap, G.N. Chaudhari, Current. Appl. Phys., 9(2009)1246.